

# femto-PIXAR: a self-supervised neural network method for reconstructing femtosecond X-ray free electron laser pulses

Gesa Goetzke\*,<sup>1</sup> Rajan Plumley\*,<sup>2,3,4</sup> Gregor Hartmann,<sup>5</sup> Tim Maxwell,<sup>4</sup> Franz-Josef Decker,<sup>4</sup> Alberto Lutman,<sup>4</sup> Mike Dunne,<sup>4</sup> Daniel Ratner<sup>†,4</sup> and Joshua J. Turner<sup>†3,4</sup>

<sup>1</sup>Deutsches Elektronen-Synchrotron (DESY), Notkestrasse 85, 22607 Hamburg, Germany

<sup>2</sup>Department of Physics, Carnegie Mellon University, Pittsburgh, PA, USA

<sup>3</sup>Stanford Institute for Materials and Energy Sciences, Stanford University, Menlo Park, CA, USA

<sup>4</sup>SLAC National Accelerator Laboratory, Menlo Park, CA, USA

<sup>5</sup>Helmholtz-Zentrum Berlin für Materialien und Energie GmbH,

Albert-Einstein-Strasse 15, 12489 Berlin, Germany

(Dated: March 12, 2025)

X-ray Free Electron Lasers (X-FELs) operate in a wide range of lasing configurations for a broad variety of scientific applications at ultrafast time-scales such as structural biology, materials science, and atomic and molecular physics. Shot-by-shot characterization of the X-FEL pulses is crucial for analysis of many experiments as well as tuning the X-FEL performance. However, for the weak pulses found in advanced configurations, e.g. those needed for coherent, two-pulse studies of quantum materials, there is no current method for reliably resolving pulse profiles. Here we show that a physics-based U-net model can reconstruct the individual pulse power profiles for sub-picosecond pulse separation without the need for simulations. Using experimental data from weak X-FEL pulse pairs, we demonstrate we can learn the pulse characteristics on a shot-by-shot basis when conventional methods fail.

## INTRODUCTION

Fluctuations in microscopic systems are directly related to their fundamental excitations – a concept dating back to Einstein’s description of the Brownian motion of pollen particles. This relationship has motivated the need for measuring fluctuations within microscopic systems to directly compare with first-principles theoretical models. However, the spatial and temporal scales of quantum systems far exceed those accessible by classical microscopy, and despite the advances in modern light sources, the energy scales pertinent to these fluctuations remain challenging to probe. One notable exception to this has been in inelastic neutron scattering, where small energy changes of scattered neutrons can be observed, and has led to understanding of dispersion in a myriad of areas, from frustrated magnets and high temperature superconductors, to biological tissue and exotic topological structures, such as skyrmions. However, the reliance of this on large crystals and its limitations with strongly absorbing elements restrict its applicability. The advent of the free electron laser has changed all of this. Its capability to generate femtosecond (fs) laser pulses with extremely high pulse energies at X-ray wavelengths has ushered in a new era of science, with new developments rapidly evolving in many fields [1, 2] including structural biology [3, 4], enzyme catalysis [5], and astrophysics [6, 7]. Furthermore, the development of coherent, two-pulse configurations brings new poten-

tial for fluctuation studies within quantum materials at their relevant timescales, i.e. at the meV energy scale and below [8–13].

Importantly, with X-FELs it is now possible to deliver coherent X-ray pulses at *sub-picosecond* spacing for experiments, resolving snapshots in structures with sub-Angstrom resolution, and comparing these scattering events to measure fluctuations, but critically, no current method exists to temporally resolve these individual incident pulses at such fine timescales. This highlights the urgent need for reliable characterization of X-FEL laser pulse intensities with femtosecond resolution. Such methods must be robust across various lasing configurations and experimental setups. Notably, X-FELs are highly sensitive to operational parameters which govern the durations, energies, and sequences of X-ray pulses [14, 15]. Compounding this complexity, X-FELs exhibit intrinsic intensity fluctuations, causing shot-to-shot variations in the pulse energy spectrum and photon density [16, 17]. These beam intensity fluctuations from the X-FEL present significant challenges for experiments where accurate characterization of pulse properties, including pulse duration and energy density, is essential to extract meaningful results. These challenges have so far hindered use of this new capability to deliver new science in the observation of fluctuations for understanding properties in materials.

We address this need by developing a novel self-supervised machine learning (ML) framework called *femto-PIXAR: femtosecond Power Inference of X-ray pulses using AI References*, which provides sufficient sensitivity to resolve microjoule-scale pulses with femtosecond pulse separation. We show our approach accurately

\* These authors contributed equally to this work

† E-mail: dratner@slac.stanford.edu, joshuat@slac.stanford.edu

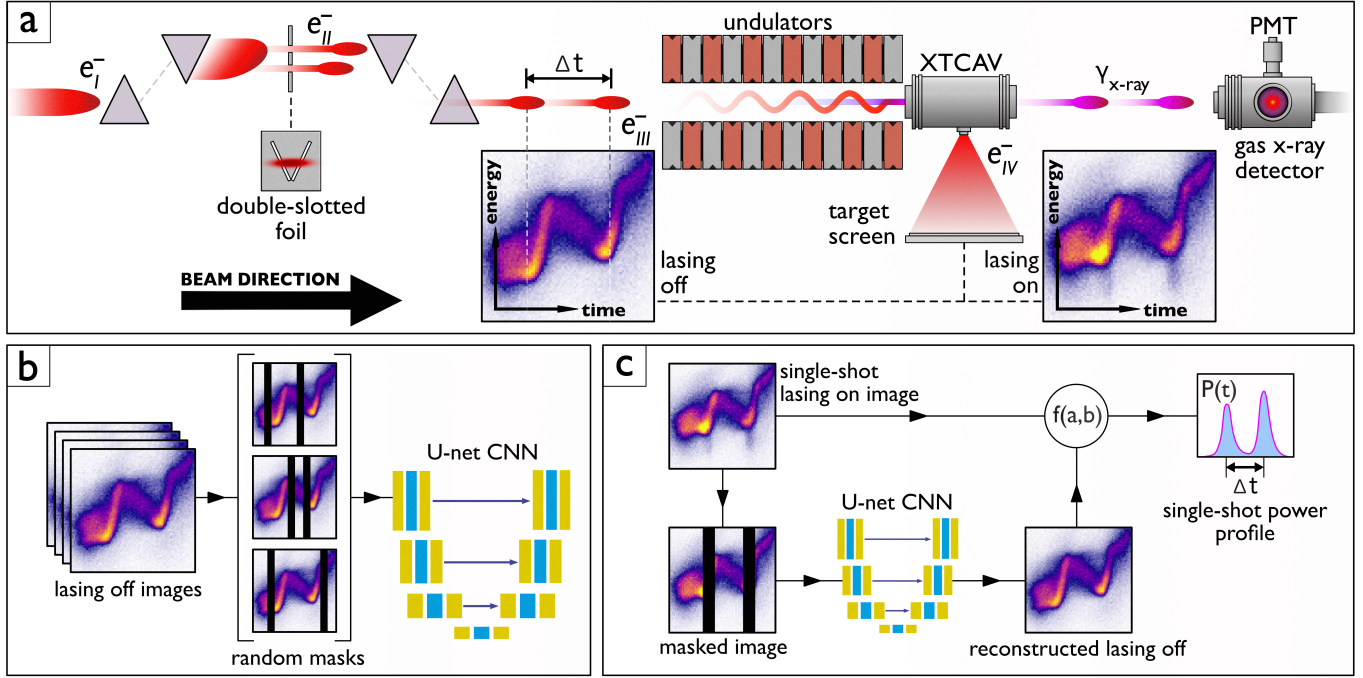


FIG. 1. (a) Diagram of the generation and shaping of a single-shot X-ray pulse pair at the LCLS, beginning with the transmission of a single electron bunch through the double-slotted foil. (b) Diagram of the ML training process. (c) Diagram of the ML-based reconstruction of the transient X-ray power profile  $P(t)$  from a single-shot lasing-on image.

predicts pulse energies for an experimental dataset, verified against total pulse energy monitors in real X-FEL data, and confirm the predictions match the expected pulse delays. This demonstration will make fluctuation studies possible in the sub-picosecond regime, and will also provide a tool for a wide array of X-FEL experiments in many other fields as well.

## SETUP

The experimental setup was designed to produce two coherent X-ray pulses starting from a single, long electron bunch, itself generated from two overlapping injector lasers. The two X-ray pulses were created using a double-slotted V-shaped foil (for time domain control) [18] [19] and hard X-ray self-seeding [20] (for coherence and energy selection). To our knowledge this configuration, described in Fig. 1 a), has never been used before. The experiment was conducted at a photon energy of 8.35 keV (Ni  $K$ -edge), with slotted-foil pulse separations of 0 fs (single pulse),  $\approx 20$  fs, and  $\approx 30$  fs. Different stages of the electron bunch shaping sequence are labeled  $e_I^-$ ,  $e_{II}^-$ ,  $e_{III}^-$ ,  $e_{IV}^-$ , representing the same electron distribution at different instances as it proceeds in time. A  $3\ \mu\text{m}$  thick aluminum foil with two slots of variable separation from 1 mm to 5 mm was placed in the middle of the dispersive section of the bunch compressor BC2 [18]. At the locations where the electron bunch  $e_I^-$  passes through the foil

the electron emittance was ‘spoiled’ (i.e. increased) due to coulomb scattering. The emittance growth suppresses FEL amplification in the undulator, so that only the electrons  $e_{II}^-$  that pass through the slits of the V-shaped foil produce X-ray pulses.

Downstream of the bunch compressor the relative distance between the unspoiled electron distributions  $e_{III}^-$  is in the direction of travel, resulting in an arrival time difference  $\Delta t$ , that can be changed by shifting the slotted foil.  $e_{IV}^-$  passes through the undulator magnets resulting in X-ray lasing. Between the first and second undulator segment a hard X-ray self-seeding scheme is applied (not shown here). Downstream of the undulators, the X-band Transverse deflecting mode CAVity (XTCAV) streaks the electron beam on a target to image the final longitudinal phase space [21]. The X-ray laser pulses are unaffected by the XTCAV deflector and continue downstream to the X-ray gas energy monitor (GEM), where the total X-ray pulse energy is transmissively monitored on a shot-to-shot basis using a photomultiplier tube (PMT) to measure the fluorescence induced in a small volume of  $\text{N}_2$  gas [22]. After the GEM, the X-rays continue down the beamline to the experimental endstations. This entire process repeats at a 120 Hz repetition rate.

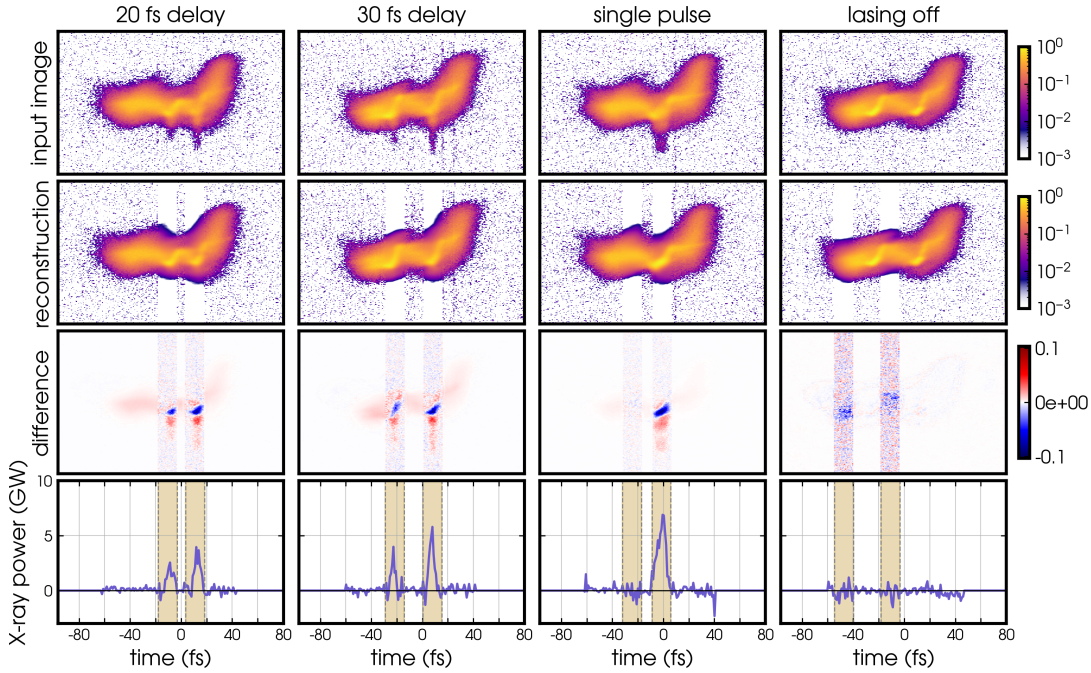


FIG. 2. Demonstration of femto-PIXAR reference creation: at the top are dark subtracted XTCAV images for three different slotted foil setups (lasing-on) and a lasing-off sample for the 30 fs delay setup; the second line shows the network’s predicted lasing-off reconstruction; the third line shows the difference image between the measured XTCAV and the reconstructed lasing-off reference; and the last line shows the reconstructed power profiles.

## DATA AND METHODOLOGY

The XTCAV images the longitudinal (time-energy) distribution of the post-lasing electron bunch. By comparison with a lasing-off reference, it is possible to infer the temporal profile of the photon pulse. However, because the lasing-on and lasing-off references cannot be measured simultaneously, this poses a fundamental challenge in determining the change in the electron phase space due to the undulators. The “classical” approach has been to record a set of images while suppressing lasing, cluster these images by shape, and then select the most similar cluster for each lasing-on image by comparing the projected electron current [21, 23, 24]. While the classical approach has been demonstrated for various two-pulse modes [14, 19, 25], it struggles for small pulse energies, when shot-to-shot differences between the true lasing-off electron bunch and the selected reference cluster exceed the lasing-induced changes. As a result, when combining seeding with two-pulse modes, the classical method breaks down.

A deep learning method proposed by Ren et al. [26] sidesteps the need for matched lasing-off references by training a neural network (NN) directly to predict power from a lasing-on image; however, the NN in [26] relies on simulated labels for training, and it is particularly challenging to simulate the complex electron beam distribution produced by the slotted foil. On the other hand, for

the slotted foil setup, only a narrow segment of the beam lases. We can exploit this feature to approximate a reference in the short lasing region by using information in the nearby non-lasing regions. For example, Zeng et al. [27] suggested to use a polynomial regression across the lasing region as a reference. However, the polynomials cannot model the complex phase space of this setup and fail to reproduce the weak lasing pulses.

Here, we instead propose an approach using a U-net [28] to generate the corresponding lasing-off reference image. We trained the NN using self-supervision, eliminating the need for simulations. Specifically, we masked regions of lasing-off pulses, and trained the NN to regenerate those regions. Once trained, the network receives a lasing-on image with masked lasing regions and reconstructs the best lasing-off reference. We then calculated the center of mass (COM) to retrieve the X-ray pulse distribution [24]. The network can also detect the lasing region by identifying areas with the largest reconstruction discrepancy. Our method provides high-fidelity lasing-off references without relying on the accuracy of computationally-expensive simulations while retaining interpretability through direct observation of the generated reference.

Fig. 1 b) and c) shows the core steps. The inputs to the network were cropped, background subtracted and normalized lasing off images, where all values within two random mask-regions were set to zero (black bars in Fig. 1 b) and c)). The width of an individual mask was chosen

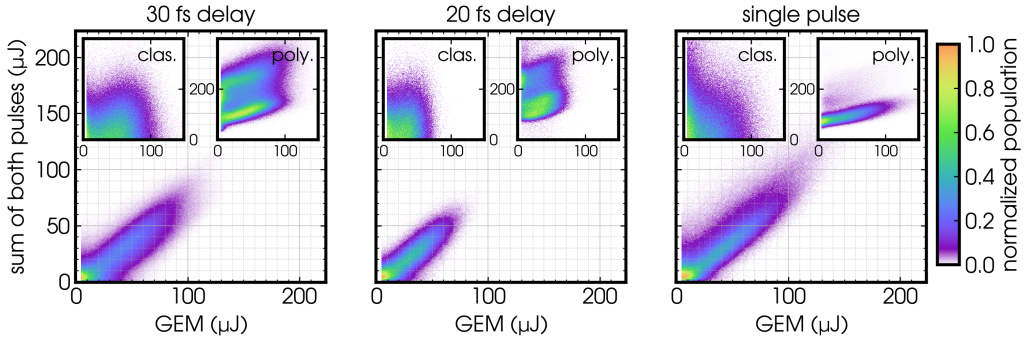


FIG. 3. Correlations with the GEM for the three different delays using the U-net approach. Both the classical method (clas.) and polynomial regression (poly.) reconstruction methods displayed in the insets show poor correlation between the predicted power-profile integrals and the total GEM pulse energy especially on the weaker double pulses ( $\approx 20$  fs and  $\approx 30$  fs delay).

to be 16 pixels and the distance range for the two masks was set from 0 to 40 pixels, corresponding to approx. 0 to 38 fs. We then trained a U-net to reconstruct the electron phase space of the lasing-off data (Fig. 1 b) ). As the center of mass is the critical value for evaluation, we used a loss that combines the Mean Squared Error of pixel values with the absolute error of the COM. After training, we masked the lasing regions in a lasing-on data set. As the network is trained only on the lasing-off data, it reconstructs the best matching lasing-off electron phase space exactly for a given image (Fig. 1 c). This lasing-off image will also exactly match the original  $x$  and  $y$  position, so no shifting in the time axis or normalization with the GEM (as in the classical approach) is necessary.

A crucial step of this process was to determine the correct mask positions in the lasing data. The separation of the two pulses was approximately fixed by the slit separation, but due to shot-to-shot differences in electron bunch energy and compression of the electron bunch, the position of the features relative to the center of mass of the electron bunch was not constant. Our method scans the image to find two locations where input and reconstruction differ most, centering the masks on the maximum signal. We then use the methods from Behrens et. al [24], marked as  $f(a, b)$  in Fig. 1 to obtain the power profile using the spectral COM from both images.

## RESULTS

Fig. 2 shows example reconstructions for the three different configurations and one lasing-off example, all randomly selected from the top 1% of data with the highest GEM values (ensuring a clearly visible signal). None of these images were part of the network training process. To demonstrate the efficacy of the proposed method, we benchmark the predicted power and delay against existing diagnostics. First, we compare the integral of the predicted profile with the total energy of both pulses measured by the GEM, which cannot resolve pulses on the fs

scale. In Fig. 3 one can see the correlation of the integral of the power profile with the GEM for the three different slotted foil configurations. We note that while there is a strong linear correlation between the predicted power and GEM monitor, there is a disagreement in proportionality. Further experiments are necessary to determine if it is due to either the GEM or XTCAV calibration, or bias from the method. However, as the typical user experiment usually relies primarily on the relative power between the pulse pairs, this discrepancy does not affect the experimental analysis.

We compare our predictions to two existing state-of-the-art XTCAV analysis methods. In order to evaluate the correlation with the GEM, in the classical approach (see the previous section), the energy jitter (shift in the  $y$ -axis) cannot be compensated for by normalization with the GEM but must instead be corrected using a scheme that matches the head and tail of the COM profiles for the lasing-on and lasing-off images. We also compare our results with the polynomial regression method of Zeng et al. [27]. Some example predictions of this method can be found in the supplemental material. Fig. 3 compares the GEM correlation for all three delays, neither of which results in the expected correlation.

Fig. 4 shows the temporal and energy characteristics of the X-ray laser pulses as retrieved by the U-net reconstruction scheme. The time assignments of each shot were obtained by fitting the X-ray power trace with two Gaussian functions. For these plots we took only the data where both Gaussian curve fits indicated a signal larger than  $15 \mu\text{J}$ . We find that the predicted time difference between both pulses closely matches the delay given by the slotted foil condition. The temporal separation jitter aligns well with the 9% jitter observed by Ding et al. [19]. As an additional benchmark we checked the predicted pulse energies for lasing-off data with randomly placed masks and find that 80% of the data has a deviation from zero of less than  $15 \mu\text{J}$ , and 99.8% less than  $25 \mu\text{J}$ .

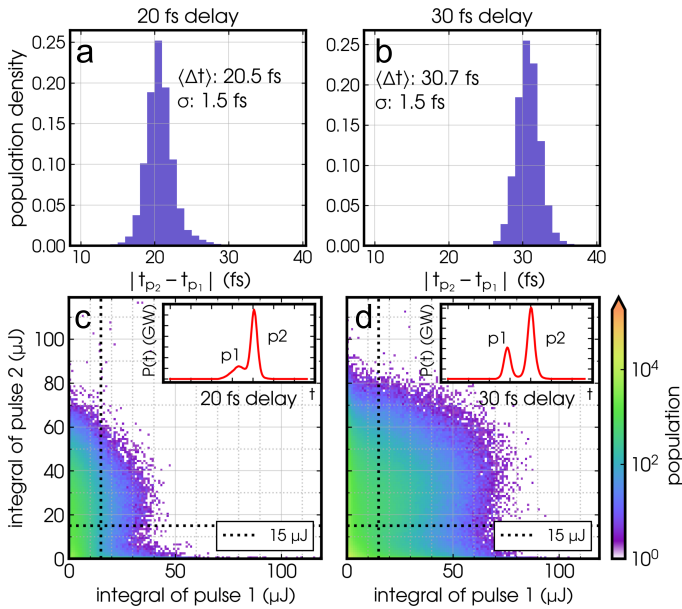


FIG. 4. (a) & (b): Histograms of temporal separation  $\Delta t$  between each pulse in time. (c) & (d): Histograms of the integrated energy in each pulse. The insets show averages of the transient X-ray power profiles, where the relative amplitudes of the pulse 1 (p1) and pulse 2 (p2) are above  $15 \mu\text{J}$ .

## DISCUSSIONS AND SUMMARY

In conclusion, femto-PIXAR is a novel X-FEL diagnostic which we demonstrate by reconstructing the X-ray power profiles from weak X-FEL pulses in a non-standard two-pulse, self-seeding configuration. For this configuration, the classical method of XTCAV analysis, which uses a matching algorithm to subtract similar lasing-off shots for the energy loss calculation, fails to reproduce meaningful correlations with the X-ray gas detector. By contrast, our method is able to distinguish the relative amplitude of each X-ray pulse on a shot-to-shot basis which is necessary for X-ray photon fluctuation spectroscopy experiments and other future experiments at X-FEL facilities. Our approach has various benefits, avoiding the need for energy calibration with an external reference. A neural network based scheme also scales well for the large datasets expected from high-throughput experiments enabled by next generation X-FEL facilities such as the LCLS-II [29]. As opposed to previous deep-learning work, our approach uses self-supervision with a physics-motivated loss function, avoiding the need for high-fidelity simulations. Our method also reconstructs the full 2D phase space, providing interpretability of the network and giving crucial information about when the network might not be applicable for a specific dataset. Future work will consider extensions to more general X-FEL configurations beyond the slotted foil. For example, using diagnostics beyond the XTCAV could enable anal-

ysis of configurations with lasing across the full electron bunch [30], e.g. to provide the femtosecond resolution needed for temporal ghost imaging [31]. The analysis chain after reconstructing the lasing-off reference can also make use of machine learning, e.g. incorporating spectral measurements to refine the X-ray pulse profile [32].

## ACKNOWLEDGMENTS

Use of the Linac Coherent Light Source (LCLS), SLAC National Accelerator Laboratory, is supported by the US Department of Energy, Office of Science, Office of Basic Energy Sciences under Contract No. DE-AC02-76SF00515. The authors acknowledge support from DESY (Hamburg, Germany). This work has in part been funded by the IVF project InternLabs-0011 (HIR3X). R. Plumley acknowledges support from the US Department of Energy, Office of Science, Basic Energy Sciences, for the Materials Sciences and Engineering Division under contract DE-AC02-76SF00515. J.J.Turner acknowledges support from the U.S. Department of Energy (DOE), Office of Science, Basic Energy Sciences under Award No. DE-SC0022216.

---

- [1] C. Bostedt, S. Boutet, D. M. Fritz, Z. Huang, H. J. Lee, H. T. Lemke, A. Robert, W. F. Schlotter, J. J. Turner, and G. J. Williams, Linac coherent light source: The first five years, *Rev. Mod. Phys.* **88**, 015007 (2016).
- [2] J. Rossbach, J. R. Schneider, and W. Wurth, 10 years of pioneering x-ray science at the free-electron laser flash at desy, *Physics reports* **808**, 1 (2019).
- [3] S. Boutet, L. Lomb, G. J. Williams, T. R. Barends, A. Aquila, R. B. Doak, U. Weierstall, D. P. DePonte, J. Steinbrener, R. L. Shoeman, *et al.*, High-resolution protein structure determination by serial femtosecond crystallography, *Science* **337**, 362 (2012).
- [4] H. N. Chapman, P. Fromme, A. Barty, T. A. White, R. A. Kirian, A. Aquila, M. S. Hunter, J. Schulz, D. P. DePonte, U. Weierstall, *et al.*, Femtosecond x-ray protein nanocrystallography, *Nature* **470**, 73 (2011).
- [5] S. L. Rose, S. V. Antonyuk, D. Sasaki, K. Yamashita, K. Hirata, G. Ueno, H. Ago, R. R. Eady, T. Toshia, M. Yamamoto, *et al.*, An unprecedented insight into the catalytic mechanism of copper nitrite reductase from atomic-resolution and damage-free structures, *Science advances* **7**, eabd8523 (2021).
- [6] S. Bernitt, G. V. Brown, J. K. Rudolph, R. Steinbrugge, A. Graf, M. Leutenegger, S. W. Epp, S. Eberle, K. Kubicek, V. Mackel, *et al.*, An unexpectedly low oscillator strength as the origin of the fe xvii emission problem, *Nature* **492**, 225 (2012).
- [7] S. M. Vinko, O. Cricosta, B. I. Cho, K. Engelhorn, H. K. Chung, C. R. Brown, T. Burian, J. Chalupsky, R. W. Falcone, C. Graves, *et al.*, Creation and diagnosis of a solid-density plasma with an x-ray free-electron laser, *Nature* **482**, 59 (2012).

[8] Y. Sun, M. Dunne, P. Fuoss, A. Robert, D. Zhu, T. Ossaka, M. Yabashi, and M. Sutton, Realizing split-pulse x-ray photon correlation spectroscopy to measure ultrafast dynamics in complex matter, *Physical Review Research* **2**, 023099 (2020).

[9] C. Gutt, L.-M. Stadler, A. Duri, T. Autenrieth, O. Leupold, Y. Chushkin, and G. Grübel, Measuring temporal speckle correlations at ultrafast x-ray sources, *Optics express* **17**, 55 (2008).

[10] R. Plumley, S. Chitturi, C. Peng, T. Assefa, N. Burdet, L. Shen, Z. Chen, A. Reid, G. Dakovski, M. Seaberg, *et al.*, On ultrafast x-ray scattering methods for magnetism, *Advances in Physics: X* **9**, 2423935 (2024).

[11] M. Seaberg, B. Holladay, J. Lee, M. Sikorski, A. Reid, S. Montoya, G. Dakovski, J. Koralek, G. Coslovich, S. Moeller, *et al.*, Nanosecond x-ray photon correlation spectroscopy on magnetic skyrmions, *Physical Review Letters* **119**, 067403 (2017).

[12] M. Seaberg, B. Holladay, S. Montoya, X. Zheng, J. Lee, A. Reid, J. Koralek, L. Shen, V. Esposito, G. Coslovich, *et al.*, Spontaneous fluctuations in a magnetic fe/gd skyrmion lattice, *Physical Review Research* **3**, 033249 (2021).

[13] W. Roseker, S. Hruszkewycz, F. Lehmkühler, M. Walther, H. Schulte-Schrepping, S. Lee, T. Ossaka, L. Strüder, R. Hartmann, M. Sikorski, *et al.*, Towards ultrafast dynamics with split-pulse x-ray photon correlation spectroscopy at free electron laser sources, *Nature communications* **9**, 1704 (2018).

[14] F.-J. Decker, K. L. Bane, W. Colocho, S. Gilevich, A. Marinelli, J. C. Sheppard, J. L. Turner, J. J. Turner, S. L. Vetter, A. Halavanau, *et al.*, Tunable x-ray free electron laser multi-pulses with nanosecond separation, *Scientific Reports* **12**, 3253 (2022).

[15] F.-J. Decker, W. Colocho, A. Halavanau, A. Lutman, J. MacArthur, G. Marcus, R. Margraf, J. Sheppard, J. Turner, and S. Vetter, *Two and Multiple Bunches with the LCLS Copper Linac*, Tech. Rep. (SLAC National Accelerator Lab., Menlo Park, CA (United States), 2022).

[16] R. Bonifacio, L. De Salvo, P. Pierini, N. Piovella, and C. Pellegrini, Spectrum, temporal structure, and fluctuations in a high-gain free-electron laser starting from noise, *Physical review letters* **73**, 70 (1994).

[17] Y. Sun, F.-J. Decker, J. Turner, S. Song, A. Robert, and D. Zhu, Pulse intensity characterization of the lcls nanosecond double-bunch mode of operation, *Journal of synchrotron radiation* **25**, 642 (2018).

[18] P. Emma, M. Borland, and Z. Huang, Attosecond x-ray pulses in the lcls using the slotted foil method, in *Proc. FEL'04. Trieste, Italy* (JACoW Publishing, pp. 333–338., 2004).

[19] Y. Ding, C. Behrens, R. Coffee, F.-J. Decker, P. Emma, C. Field, W. Helml, Z. Huang, P. Krejcik, J. Krzywinski, H. Loos, A. Lutman, A. Marinelli, T. J. Maxwell, and J. Turner, Generating femtosecond x-ray pulses using an emittance-spoiling foil in free-electron lasers, *Applied Physics Letters* **107**, 191104 (2015).

[20] J. Amann, W. Berg, V. Blank, F.-J. Decker, Y. Ding, P. Emma, Y. Feng, J. Frisch, D. Fritz, J. Hastings, Z. Huang, J. Krzywinski, R. Lindberg, H. Loos, A. Lutman, H.-D. Nuhn, D. Ratner, J. Rzepiela, D. Shu, Y. Shvyd'ko, S. Spampinati, S. Stoupin, S. Terentyev, E. Trakhtenberg, D. Walz, J. Welch, J. Wu, A. Zholents, and D. Zhu, Demonstration of self-seeding in a hard-x-ray free-electron laser, *Nature Photonics* **6**, 693 (2012).

[21] Y. Ding, C. Behrens, P. Emma, J. Frisch, Z. Huang, H. Loos, P. Krejcik, and M.-H. Wang, Femtosecond x-ray pulse temporal characterization in free-electron lasers using a transverse deflector, *Physical Review Special Topics - Accelerators and Beams* **14**, 120701 (2011).

[22] S. P. Hau-Riege, R. M. Bionta, D. D. Ryutov, R. A. London, E. Ables, K. I. Kishiyama, S. Shen, M. A. McKernan, D. H. McMahon, M. Messerschmidt, *et al.*, Near-ultraviolet luminescence of n 2 irradiated by short x-ray pulses, *Physical review letters* **105**, 043003 (2010).

[23] T. J. Maxwell, C. Behrens, Y. Ding, Z. Huang, P. Krejcik, A. Marinelli, L. Piccoli, and D. Ratner, Femtosecond-scale x-ray FEL diagnostics with the LCLS x-band transverse deflector, in *SPIE Proceedings*, edited by S. P. Hau-Riege, S. P. Moeller, and M. Yabashi (SPIE, 2014).

[24] C. Behrens, F.-J. Decker, Y. Ding, V. A. Dolgashev, J. Frisch, Z. Huang, P. Krejcik, H. Loos, A. Lutman, T. J. Maxwell, J. Turner, J. Wang, M.-H. Wang, J. Welch, and J. Wu, Few-femtosecond time-resolved measurements of x-ray free-electron lasers, *Nature Communications* **5**, 10.1038/ncomms4762 (2014).

[25] A. Marinelli, R. Coffee, F.-J. Decker, Y. Ding, R. Field, S. Gilevich, Z. Huang, D. Kharakh, H. Loos, A. Lutman, T. Maxwell, J. Turner, and S. Vetter, Twin-bunch two-colour fel at lcls, *Proceedings of the 7th Int. Particle Accelerator Conf. IPAC2016*, Korea (2016).

[26] X. Ren, A. Edelen, A. Lutman, G. Marcus, T. Maxwell, and D. Ratner, Temporal power reconstruction for an x-ray free-electron laser using convolutional neural networks, *Physical Review Accelerators and Beams* **23**, 040701 (2020).

[27] L. Zeng, C. Feng, D. Gu, X. Wang, K. Zhang, B. Liu, and Z. Zhao, Online single-shot characterization of ultrafast pulses from high-gain free-electron lasers, *Fundamental Research* **2**, 929 (2022).

[28] O. Ronneberger, P. Fischer, and T. Brox, U-net: Convolutional networks for biomedical image segmentation, in *Medical Image Computing and Computer-Assisted Intervention (MICCAI)*, LNCS, Vol. 9351 (Springer, 2015) pp. 234–241, (available on arXiv:1505.04597).

[29] J. N. Galayda, *The LCLS-II: A high power upgrade to the LCLS*, Tech. Rep. (SLAC National Accelerator Lab., Menlo Park, CA (United States), 2018).

[30] A. Sanchez-Gonzalez, P. Micaelli, C. Olivier, T. Barillot, M. Ilchen, A. Lutman, A. Marinelli, T. Maxwell, A. Achner, M. Agåker, *et al.*, Accurate prediction of x-ray pulse properties from a free-electron laser using machine learning, *Nature communications* **8**, 15461 (2017).

[31] D. Ratner, J. Cryan, T. Lane, S. Li, and G. Stupakov, Pump-probe ghost imaging with sase fels, *Physical Review X* **9**, 011045 (2019).

[32] D. Ratner, F. Christie, J. Cryan, A. Edelen, A. Lutman, and X. Zhang, Recovering the phase and amplitude of x-ray fel pulses using neural networks and differentiable models, *Optics express* **29**, 20336 (2021).

[33] S. Marholm, sigvaldm/localreg: Multivariate rbf output (2022).

## Supplemental Materials

### A1: DATA PREPARATION

The centered XTCAV images have a shape of  $240 \times 240$  pixel. A median dark image is subtracted and they are normalized to have intensities roughly between 0 and 1 before they are used in the network. Before obtaining the power profiles a median filter is used to identify the signal region and set the other regions to zero. This approach is just used to identify the signal region, no median operation is applied to the image.

### A2: NETWORK ANALYSIS

We used an U-net architecture as described in [28]. The optimizer is RMSprop of pytorch with a weight decay of  $1e-8$ . Out of some manual tries, we picked a learning rate of  $5e-7$  and a batch size of 2. We found that we get good reconstructions with this parameter set. A more extensive hyper parameter search might provide slightly better reconstructions or faster conversion of the network. However we found that the data preparation like scaling and centering is way more important than the exact hyper parameters. For the loss we used an MSE loss on the reconstruction, combined with an absolute error on the COM. The COM has a relative low weight of  $1e-4$  as we found that higher weights significantly worsen the reconstruction.

In all our lasing-on datasets we exclude images with weak XGMD signal ( $< 5 \mu\text{J}$ ). With this threshold we discarded about 15% of our data, resulting in about  $4 \times 10^5$  samples with approx. 20 fs difference, about  $1.5 \times 10^6$  samples with approx. 30 fs difference and  $9 \times 10^4$  with only one pulse. Weak shots (where essentially no lasing occurs) with  $E_{\text{GMD}} < 5 \mu\text{J}$  are included in the lasing-off dataset to get more training data. This results in about 30K lasing-off samples.

### A3: CLASSICAL ANALYSIS

For the classical analysis the signal region is identified as described in Appendix A, and then divided into 120 slices so that all lasing-on and lasing-off data has the same length in slices and lasing-on and lasing-off data can be compared directly. HierarchicalClustering (sklearn.cluster.AgglomerativeClustering) with euclidean distance is used to cluster the current profiles into 500 groups. Normally, a few hundred lasing-offs are used to build a reference set, but to have a fairer comparison all lasing-off images that are used in the training of the network are provided to the algorithm. The COM

profile of these groups are averaged and used as reference.

### A3: IMPLEMENTATION OF POLYNOMIAL REGRESSION METHOD

For the polynomial regression we used an algorithm described in [33]. Zeng et al. [27] uses a 13 dimensional polynomial, we find that our algorithm does not converge in this case. In Fig. A1 we show one example of the regression method with increasing polynomial degrees. In our benchmark we use the highest degree where the algorithm converges, with a maximum of 13. In Fig. A2 we show resulting regressions for ten different samples. We found that the predictions have a better correlation with the XGMD if we ignore the (obvious wrong) parts of the predicted profile that are negative.

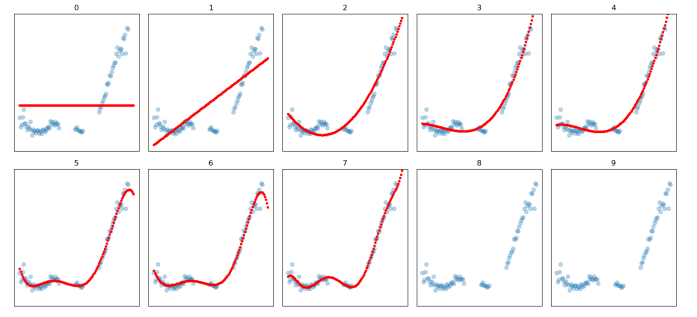


FIG. A1. The blue dots mark the COM for one sample. The COM within the mask region is reconstructed with increasing polynomial degrees. For a degree higher larger seven, it does not converge.

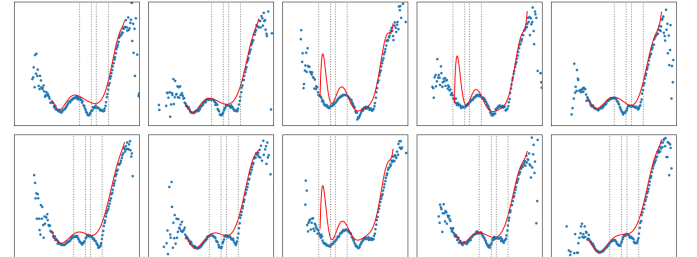


FIG. A2. Resulting regression profiles for ten different samples. In case c) and h) the regression predicts additional maxima. In all cases it does not follow the drop completely. Therefore this approach produces a higher spread and an offset compared to the XGMD benchmark.

### A4: RESIDUAL ERROR BENCHMARK

An additional method to benchmark our method is to evaluate the generated power profiles for data where no

lasing process took place. Ideally, for this setup, the integral of the power profiles would be zero. Fig. A3 shows a histogram of the resulting energies of 4600 non-lasing data points. We used 460 lasing-off samples that were not part of the network training and used each of them 10 times with randomly set masks. 80% of the data has a deviation from zero of less than  $15 \mu\text{J}$ , 99.8 % less than  $25 \mu\text{J}$ . As we are interested in the pulse ratio between the two peaks it is important that not one of the pulses is systematically under and the other over estimated. We check this on the right side of Fig. A3 and see that the pulse energy difference between the two pulses is centered well around zero. This indicates, that, for this dataset, not one pulse is overestimated over the other.

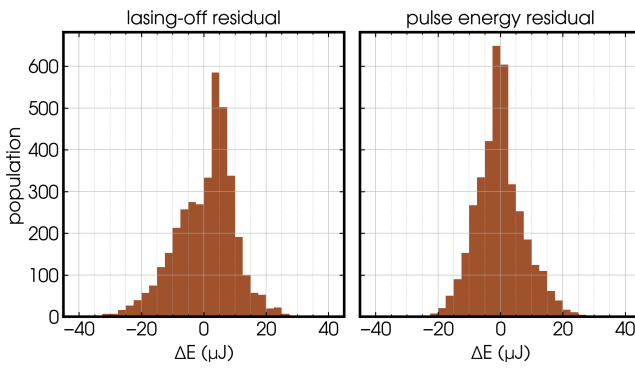


FIG. A3. Histogram of the deviation from zero of the derived sum energy of lasing-off power profile predictions. On the left you can see the sum of the integral of the Gaussian fits of both power profiles, on the right the difference between the first and the second peak. The sum is biased towards the positive side as the starting values for the Gaussian fits are positive.

#### A5: TIME DISTRIBUTION EXTRACTED FROM RECONSTRUCTED PROFILES

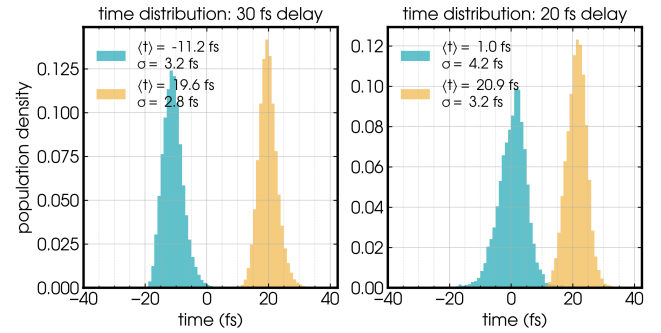


FIG. A4. Distribution of pulse arrival times from both two-pulse setups.  $t = 0$  is defined by the center of mass of the XTCAV spectrograph.

Using a double-Gaussian fit over the reconstructed transient X-ray power profiles, we are able to determine the arrival times of the two pulses at the XTCAV target. The time axis in A4 is centered with respect to the COM of the spectrograph in the temporal domain. The reconstructed pulses obtained by the Gaussian fits produce bimodal time distributions that match the X-FEL setups, with average time jitter of 3.3 fs.